Probing the Stability of SrIrO$_3$ During Active Water Electrolysis via Operando Atomic Force Microscopy

Andrew R. Akbashev,[1,2,5]* Vladimir Roddatis,[3] Christoph Baeumer,[1,2,4] Tianchi Liu,[1] J. Tyler Mefford,[1,2] William C. Chueh[1,2]

[1]Department of Materials Science and Engineering, Stanford University, Stanford, CA 94305, USA.

[2]Stanford Institute for Materials and Energy Sciences, SLAC National Accelerator Laboratory, Menlo Park, CA 94025, USA.

[3]German Research Centre for Geosciences GFZ, Helmholtz Centre Potsdam, 14473 Potsdam, Germany.

[4]Institute of Electronic Materials (IWE2) and JARA-FIT, RWTH Aachen University, 52062 Aachen, Germany.

[5]Present address: Division for Research with Neutrons and Muons, Paul Scherrer Institute, 5232 Villigen, Switzerland

* Corresponding authors: andrei.akbasheu@psi.ch

Mechanistic studies of oxide electrocatalysts for heterogeneous water oxidation have been primarily focused on understanding the origins of activity, with fewer studies studying fundamental properties influencing stability. The main challenge is directly observing and quantifying local structural instability under operating conditions. In this work, we provide a dynamic view of the perovskite stability as a function of time and operational voltage using *operando* electrochemical atomic force microscopy (EC-AFM). Specifically, we study the degradation pathways of SrIrO$_3$, a highly active electrocatalyst, during the oxygen evolution reaction (OER) by tracking the potential-dependent Sr leaching and perovskite dissolution at the nanometer scale. This material serves as a model system for degradation studies of perovskite AMO$_3$ oxides, exhibiting both A-cation leaching and transition metal (M) dissolution. We show that Sr leaching precedes perovskite dissolution by up to 0.8 V, leading to a wide voltage window of stability where water oxidation occurs on a Sr-depleted surface without significant corrosion. Moreover, we reveal that the stability of the perovskite surface is strongly influenced by the electrolytic environment and that corrosion rates differ dramatically as a function of dissolved Sr concentration. Ultimately, our study demonstrates
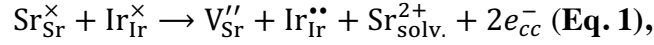
the overall stability of perovskite oxides during electrocatalysis can be substantially improved by suppressing A-site leaching.

Introduction

During water electrolysis, hydrogen is produced through electrochemical reduction of water at the cathode while the anode oxidizes water to oxygen via the oxygen evolution reaction (OER). Due to their high activity, perovskite oxides containing transition metals are among the most attractive electrocatalytic materials for water oxidation.[1,2] However, during OER, perovskites experience corrosive degradation through the formation of oxidized and water-soluble transition metal species on the surface.[3–10] A lack of fundamental understanding of how structure and composition of perovskite surfaces evolves during OER and which mechanisms drive their electrochemical degradation poses a significant challenge to the development of stable and active electrocatalysts.[11–14]
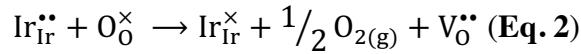
Several major pathways for the electrochemical degradation of perovskite electrocatalysts have been proposed. First, selective leaching of alkali-earth metals during the OER on perovskite surfaces is ubiquitous. Under oxidative conditions, such A-site cation-depleted surface layers eventually drive structural transformation and amorphization[3,4]. Second, oxidative dissolution of transition metals from oxide surfaces is often observed at high overpotentials[7,13,15,16]. The rate of such anodic dissolution strongly depends on the chemical composition[7,12,17–19], structure[19,20] and crystallographic orientation[16] (facet) of the oxide surface. Finally, the evolution of lattice oxygen modifies the ligand coordination of surface transition metal ions, becoming an additional factor in the degradation of a perovskite.[21–23] For clarity, we define leaching as an ion de-insertion process that preserves the structural motif of an oxide (i.e., a topochemical reaction involving vacancies), while dissolution is a complete structural disintegration of the surface layer through the solvation of the transition metal ions.

Strontium iridate ($SrIrO_3$) has recently attracted attention owing to its exceptionally high OER activity proposed to originate through Sr^{2+} leaching and surface amorphization.[3,7,8,10,24–28] Assuming that Sr^{2+} leaching involves electrochemical de-insertion (Path 1 as opposed to Path 2 in **Equations S1**), electrochemical leaching of Sr^{2+} from $SrIrO_3$ involves two holes ($h^{\bullet}$). The reaction in the Kröger-Vink notation is as follows (see also Equations S1):

$$\text{Sr}_{\text{Sr}}^{\times} + \text{Ir}_{\text{Ir}}^{\times} \longrightarrow \text{V}_{\text{Sr}}'' + \text{Ir}_{\text{Ir}}^{\bullet\bullet} + \text{Sr}_{\text{solv.}}^{2+} + 2e_{cc}^{-} \ \textbf{(Eq. 1)},$$
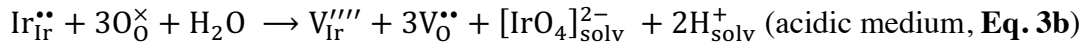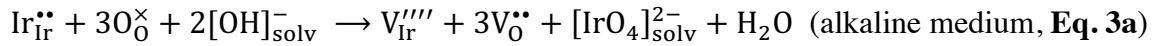
where "cc" means current collector and "solv" means the species is in the solvated state (in solution). This reaction creates a surface layer of $\text{Sr}_{1-x}\text{IrO}_3$ proposed to contain Ir(VI). Previous studies showed that Sr leaching leads to the formation of an OER-active defect-rich IrO_x surface layer in acidic electrolytes[8,10].

Depending on pH and applied potential, additional reactions may occur after Sr leaching. One possibility is that the Sr-deficient layer evolves lattice oxygen chemically (no net electron transferred) via the reaction that restores Ir(IV) within the near-surface layer:

$$\text{Ir}_{\text{Ir}}^{\bullet\bullet} + \text{O}_{\text{O}}^{\times} \longrightarrow \text{Ir}_{\text{Ir}}^{\times} + {}^{1}\!/_{2}\,\text{O}_{2(\text{g})} + \text{V}_{\text{O}}^{\bullet\bullet} \ \textbf{(Eq. 2)}$$

When put together, Equations 1 and 2 comprise the formation of a partial Schottky defect $\text{V}_{\text{Sr}}''+\text{V}_{\text{O}}^{\bullet\bullet}$. Another possibility is that $\text{Ir}_{\text{Ir}}^{\bullet\bullet}$ dissolves chemically through the solvation of the $[\text{IrO}_4]^{2-}$ species:

$$\text{Ir}_{\text{Ir}}^{\bullet\bullet} + 3\text{O}_{\text{O}}^{\times} + 2[\text{OH}]_{\text{solv}}^{-} \longrightarrow \text{V}_{\text{Ir}}'''' + 3\text{V}_{\text{O}}^{\bullet\bullet} + [\text{IrO}_4]_{\text{solv}}^{2-} + \text{H}_2\text{O} \ \ (\text{alkaline medium, } \textbf{Eq. 3a})$$

$$\text{Ir}_{\text{Ir}}^{\bullet\bullet} + 3\text{O}_{\text{O}}^{\times} + \text{H}_2\text{O} \longrightarrow \text{V}_{\text{Ir}}'''' + 3\text{V}_{\text{O}}^{\bullet\bullet} + [\text{IrO}_4]_{\text{solv}}^{2-} + 2\text{H}_{\text{solv}}^{+} \ (\text{acidic medium, } \textbf{Eq. 3b})$$

One can note that adding **Equation 1 and 3** yields the electrochemical dissolution reaction under the assumption that the vacancies are generated at the surface and become eliminated as a lattice unit. Although several scenarios have been proposed previously[14,17,18,29], the mechanism involving the dissolution of Ir(VI) oxide is the most probable at high potentials because IrO_3 is volatile and soluble in water[30–32]. Anodic dissolution of iridium during OER was observed for both metallic iridium[12,17,33–35] and Ir-containing oxides such as hydrous/amorphous[11,19,35] and rutile IrO_2 (ref. [11,12,19,33]), perovskite SrIrO_3,[19] double-perovskite $\text{Sr}_2\text{CoIrO}_6$ [7] and $\text{Ba}_2\text{PrIrO}_6$ [19]. We also note that this scenario can lead to the growth of amorphous and possibly hydrated IrO_x on the surface via a precipitation reaction[7].

While Sr leaching and iridium dissolution have been investigated separately, the coupling between the two processes is poorly understood because both Sr leaching and surface evolution are inherently dynamic processes and cannot be characterized using *post mortem* measurements

that provided a static (*ex situ*) insight. Employing $SrIrO_3$ as a model system, in this work we study the oxidative electrochemical behavior of a perovskite electrocatalyst in real time, demonstrating that corrosion of a perovskite is not a simple "layer-by-layer" process hypothesized earlier[36] but involves many processes that precede dissolution and influence activity and stability. We reveal that the perovskite dissolution initiates at potentials that are significantly higher than those for Sr leaching. Moreover, we show that the dissolution can be controlled by suppressing the Sr leaching rate using the Sr^{2+}-containing electrolyte.

Experimental results

Single-crystalline surfaces were prepared by depositing $SrIrO_3$ epitaxial thin films on Nb-doped (001) $SrTiO_3$ substrates using pulsed laser deposition. The samples were grown in a layer-by-layer mode and exhibit high crystalline quality and step terraces at the surface. To quantify film thickness in AFM experiments, we fabricated a $Sr_3Al_2O_6$ lift-off pattern prior to $SrIrO_3$ deposition, creating a sharp step between the film and the substrate (**Figure S3**). As our samples showed a potential-dependent solid-state junction resistance, no iR correction was performed on the electrochemical data, which affects mostly the potential regions involving high currents and measured in the rotating disk electrode (RDE) cell (specific values for the solution resistance are in Methods).

First, we performed cyclic voltammetry in 0.1M KOH (pH = 12.8) and 0.5M H_2SO_4 (pH = 0.29) electrolytes followed by *ex-situ* AFM to characterize the surface morphology (**Figure 1**). In KOH, the dissolution of $SrIrO_3$ starts at the observable onset of OER (1.45 V *vs* RHE, Reversible Hydrogen Electrode), as evidenced by the decrease in film thickness (**Figure S7**). Importantly, AFM images show that the step terraces remain topographically preserved, and electrochemical dissolution does not follow a step retreat[37,38] or etch pit formation[39,40] which are prevalent during chemical dissolution of crystals. Instead, the film dissolves uniformly, with step terraces remaining topographically visible even after the total height loss of 5 nm (**Figure 1c-g, S6** and **S7**), with roughness simultaneously increasing with the amount of dissolved film (**Figure 1b**). In H_2SO_4, on the other hand, no dissolution is observed under these potentials (as shown by operando EC-AFM and discussed below). Instead, particulates appear at ~1.17 V and disappear at 1.5-1.6 V (**Figure 1h-l**). Most of such particulates are < 5 nm in size, but some reach over 20 nm. These particulates noticeably impact the surface roughness (**Figure 1b**) but do not change the overall step-terraced

morphology. We note that some particulates were observed in KOH as well, but they were more sparsely distributed than in H_2SO_4.

Next, we employed *operando* EC-AFM to track the dissolution kinetics of $SrIrO_3$ by quantifying the potential-dependent topography and thickness. Specifically, the tip scans fast perpendicular to the edge between the exposed substrate region and $SrIrO_3$ electrode and generates a height profile of the film relative to the substrate. The slow scan direction is parallel to the edge and is correlated in time to the concurrent linear sweep voltammetry (LSV) measurement (**Figure S3b**). In KOH, as the potential reaches 1.3-1.4 V, the $SrIrO_3$ surface develops particulates that extend tens of nm laterally and only few nm in height (**Figure 2a-b, S9**). These particulates are immobile when scanned with an AFM tip and disappear as $SrIrO_3$ starts to dissolve at ~2 V (**Figure 2a, S9, S11, S12**). We speculate that these particulates are $SrCO_3$, a reaction product between leached Sr^{2+} and dissolved CO_3^{2-}. The CO_3^{2-} species are dominant at high pH[41] and originate from the dissolved CO_2 in the electrolyte that is exposed to air. At pH = 12.8, the Sr^{2+} solubility (in equilibrium with $SrCO_3$) is only $23\mu M$. Another possibility is chemical precipitation[42,43] of $IrO_x \cdot nH_2O$ at high pH from the hydrolyzed species of Ir(III) or Ir(IV) (such as $[Ir(OH)_5(H_2O)]^{2-}$ or $[Ir(OH)_6]^{2-}$). However, we do not see such particulates at higher potentials when the concentration of anodically dissolved iridium reaches the highest value in the solution.

In H_2SO_4, the behavior of $SrIrO_3$ is markedly different. **Figure 2d** shows the evolution of the topography, thickness, and current density during a slow LSV sweep measured with EC-AFM. The particulates appear at potentials close to open-circuit and remain on the surface until ~1.45 V (**Figure 2e**), consistent with *ex-situ* AFM imaging (**Figure 1h-l**). We propose that these particulates are $SrSO_4$, with the solubility limit of Sr^{2+} being $24\mu M$.

Finally, we turn our attention to the evolution of the electrode thickness. The potential-dependent dissolution rates in both alkaline and acidic electrolytes extracted from the AFM data are plotted in **Figure 2g**. The onset potential of dissolution in KOH is 1.9-2.0 V, with the rates reaching 0.2 Å/s at 2.3 V. In H_2SO_4 the onset potential is substantially higher at 2.4 V.

To understand the evolution of chemical composition in the near-surface layer, we performed X-ray photoelectron spectroscopy (XPS) after a 5-min potentiostatic hold at different potentials spanning both the pre-catalytic and OER regions. We note that XPS can show slightly skewed Sr:Ir ratio due to the abundant particulates on the surface that contribute to the overall Sr signal. In XPS, the Sr:Ir molar ratio was probed for two distinct mean escape depths (MED): (i)

surface region having MED ≈ 12 Å for Sr and 12 Å for Ir, and (ii) thicker (deeper) surface layer with MED ≈ 23 Å for Sr and 24 Å for Ir. Specifically, we found that Sr leaching in KOH proceeds from 1.3 to 1.5 V, after which the Sr:Ir ratio levels off and remains constant (**Figure 2h**). The loss of Sr coincides with the appearance of particulates on the surface, consistent with our hypothesis of a "leaching-precipitation mechanism" whereby a critical concentration of leached Sr^{2+} reacts with CO_3^{2-} to form $SrCO_3$. Most crucially, Sr leaching occurs at a potential ~0.3V lower than the onset of dissolution.

In H_2SO_4, Sr leaching is also observed but it does not level off with potential (**Figure 2h**). Instead, the Sr:Ir ratio at MED ≈ 12 Å decreases to 0.35 close to the onset of dissolution at 2.3 V, forming a substantially more Sr-depleted surface than in KOH. The inset in **Figure 2h** shows high-angle annular dark-field (HAADF) scanning transmission electron microscopy (STEM) images and the distribution of Sr and Ir obtained by mapping the electron energy loss spectra (EELS) in the film after the last measurement. The images reveal a highly disordered strontium-deficient $Sr_{1-x}IrO_{3-y}$ layer (~3-4 nm thick) on top of $SrIrO_3$. These results directly correlate with the XPS data. Similar layers were observed previously for $SrIrO_3$ in $HClO_4$ [27] and H_2SO_4 [8,10,24]. Importantly, by comparing **Figure 2g** and **Figure 2h**, we observe a large potential gap (~0.6 V) between Sr leaching and perovskite dissolution.

To probe the bulk dissolution process, we perform *operando* EC-AFM galvanostatically at 10 mA/cm² in both alkaline and acidic electrolytes. The potential required to drive such high currents in the AFM liquid cell is greater than the potential measured in the RDE experiments due to uncompensated resistance losses in the constrained geometry inside the AFM cell. In KOH, the film dissolution rate measured directly via *operando* EC-AFM is ~0.1 Å/s and remains constant with thickness (**Figure 3a**). Particulates like those observed in slow LSV appear immediately after the potential is reached (**Figure S13 and S14**). In H_2SO_4, on the other hand, EC-AFM shows no detectable dissolution of the film over a period of 80 min (**Figure 3b, S15**), indicating a much higher stability at 10 mA/cm² than in the case of alkaline electrolyte.

In the final set of experiments, we test our hypothesis that Sr leaching promotes a faster dissolution of the perovskite phase. Specifically, we measure nominally identical $SrIrO_3$ electrodes (30 nm thick) galvanostatically at 10 mA/cm² in various electrolytes using a rotating disk electrode in a large volume cell (**Figure 3c**). A rapid increase of potential beyond 3V indicates a complete dissolution of the film. First, we perform these experiments in KOH and H_2SO_4. In KOH, $SrIrO_3$

shows a short 60-min plateau at ~1.8 V, indicating that the dissolution rate is 0.08 Å/s and consistent with the EC-AFM results. In H_2SO_4, the film shows two plateaus: one at ~1.67 V with a longer stability than in the basic electrolyte and the second plateau at ~2.32 V that continues for ~500 min. The resulting dissolution rate of 0.006 Å/s is ~10 times smaller than in KOH and correlates well with a negligible dissolution rate reported for IrO_2 in acids[12,22,33]. Next, we hypothesized that Sr leaching can be suppressed by decreasing the Sr chemical potential difference between the film and electrolyte. To do so, we use a 0.05M $Sr(OH)_2$ electrolyte which has the same pH as that of 0.1M KOH. The galvanostatic test in $Sr(OH)_2$ reveals a 2-3 times longer plateau that scales with the film thickness (**Figure 3c** and **S16**), while XPS studies indicate a larger Sr:Ir ratio than in the case of KOH and H_2SO_4 (**Figure S17**). The results of the post-mortem STEM study of the films tested galvanostatically at 10 mA/cm² for 1 h are shown in **Figure 3d-f.** In H_2SO_4 and $Sr(OH)_2$, HAADF-STEM clearly reveals a thin Sr-depleted layer at the surface of the films tested. In KOH, however, no such layer is observed.

Discussion

First, our experiments demonstrate that the onset of Sr leaching and noticeable $SrIrO_3$ dissolution are separated by a wide potential gap (0.6-0.8 V in H_2SO_4 and 0.3 V in KOH), indicating that $Sr_{1-x}IrO_{3-y}$ dissolves only after sufficient Sr leaches from the near-surface region. When compared to literature, this $Sr_{1-x}IrO_{3-y}$ layer exhibits higher anodic stability (lower dissolution rate at similar potentials) compared to Ir metal in both alkaline[34] and acidic[34] conditions, and hydrous Ir oxide in an acid[18]. Since we also see a multifold improvement of the electrode stability in the $Sr(OH)_2$ electrolyte, we conclude that the anodic stability of perovskites in alkaline electrolytes depends on the amount of Sr within the surface layer (**Figure 4**). The more Sr remains in the perovskite structure, the more stable the surface is toward dissolution. In other words, Sr leaching not only precedes perovskite dissolution, but it also controls the anodic stability during OER.

Second, our experiments show that Sr leaching occurs before OER (by ~0.3 V in H_2SO_4 and 0.1 V in KOH). These observations do not support the scenario proposed by Wan *et al*[27] whereby Sr leaching in $SrIrO_3$ happens during OER due to the lattice oxygen oxidation reaction. Instead, we propose that Sr leaching in the pre-OER region can occur via the electrochemical de-insertion of Sr^{2+} that is compensated by an increase of the Ir oxidation state (**Equation 1**).

Third, our *operando* EC-AFM experiments reveal that the SrIrO$_3$ dissolves in KOH at potentials very close to those in H$_2$SO$_4$. At a dissolution rate of 0.2 Å/s (equivalent to 50 pmol/s·cm^2), **Figure 2**, the potential difference is only 0.2 V, similar to previous observations using on-line electrochemical mass spectrometry for Ir metal[34,34] . In contrast, the Pourbaix diagram shows that the potentials that separate IrO$_2$ and [IrO$_4$]$^{2-}$ stability regions differ by as much as ~0.7 V between the acidic and basic conditions.[34,44] This implies that the dissolution of Ir-based oxides is largely governed by the kinetics and cannot be analyzed purely within a thermodynamic framework. Alternatively, different stoichiometry of proton-coupled reactions should be considered, moving the dissolution potentials closer to each other.

Finally, we comment on the variability of long-term stability of the SrIrO$_3$ electrodes reported in literature. In previous studies, different behaviors of SrIrO$_3$ films in acidic electrolytes have been reported, including (i) a small increase of activity during the first sweeps followed by degradation[8], (ii) a moderate and continuous increase in activity without any noticeable dissolution of the film[27], (iii) a significant increase of activity during a galvanostatic test[10]. In our study, we do not see activity improvement in either prolonged cycling or galvanostatic tests (**Figure S5** and **S16**). While the reasons for such drastically different behavior of SrIrO$_3$ is unknown, it could be related to a high sensitivity of the surface chemical composition to the deposition conditions of oxide films.[45]

Conclusion

In this study, we use *operando* EC-AFM to characterize the surface and thickness evolution of model SrIrO$_3$ electrocatalysts. We quantify the potential-dependent dissolution rate with a sub-nanometer precision across a wide potential range extending deep into the OER region. Our study illustrates the complexity of the pH-dependent interplay between the perovskite dissolution kinetics and Sr leaching during OER. Importantly, we reveal that Sr leaching precedes the net perovskite dissolution by > 0.6V in H$_2$SO$_4$ and 0.3 V in KOH. By inhibiting Sr leaching in the Sr(OH)$_2$ electrolyte, we demonstrate that the lifetime of the perovskite electrocatalyst is noticeably improved. Our work not only develops new methods for studying the kinetics of electrochemical degradation of oxides, but also shows that the control over the A-site leaching is a viable strategy for achieving improved stability of perovskite electrocatalysts.

References

1.   Hwang, J. *et al*. Perovskites in catalysis and electrocatalysis. *Science* **358**, 751–756 (2017).

2.   Hong, W. T. *et al*. Toward the rational design of non-precious transition metal oxides for oxygen electrocatalysis. *Energy Environ. Sci.* **8**, 1404–1427 (2015).

3.   May, K. J. *et al*. Influence of Oxygen Evolution during Water Oxidation on the Surface of Perovskite Oxide Catalysts. *J. Phys. Chem. Lett.* **3**, 3264–3270 (2012).

4.   Fabbri, E. *et al*. Dynamic surface self-reconstruction is the key of highly active perovskite nano-electrocatalysts for water splitting. *Nat. Mater.* **16**, 925 (2017).

5.   Chang, S. H. *et al*. Functional links between stability and reactivity of strontium ruthenate single crystals during oxygen evolution. *Nat. Commun.* **5**, 4191 (2014).

6.   Akbashev, A. R. *et al*. Activation of ultrathin $SrTiO_3$ with subsurface $SrRuO_3$ for the oxygen evolution reaction. *Energy Environ. Sci.* **11**, 1762–1769 (2018).

7.   Zhang, R. *et al*. A Dissolution/Precipitation Equilibrium on the Surface of Iridium-Based Perovskites Controls Their Activity as Oxygen Evolution Reaction Catalysts in Acidic Media. *Angew. Chem. Int. Ed.* **58**, 4571–4575 (2019).

8.   Song, C. W., Suh, H., Bak, J., Bae, H. B. & Chung, S.-Y. Dissolution-Induced Surface Roughening and Oxygen Evolution Electrocatalysis of Alkaline-Earth Iridates in Acid. *Chem* **5**, 3243–3259 (2019).

9.   Zhang, R. *et al*. Importance of Water Structure and Catalyst–Electrolyte Interface on the Design of Water Splitting Catalysts. *Chem. Mater.* **31**, 8248–8259 (2019).

10.   Seitz, L. C. *et al*. A highly active and stable IrO_x/$SrIrO_3$ catalyst for the oxygen evolution reaction. *Science* **353**, 1011 (2016).

11.   Danilovic, N. *et al*. Activity–Stability Trends for the Oxygen Evolution Reaction on Monometallic Oxides in Acidic Environments. *J. Phys. Chem. Lett.* **5**, 2474–2478 (2014).

12.   Cherevko, S. *et al*. Oxygen and hydrogen evolution reactions on Ru, RuO_2, Ir, and IrO_2 thin film electrodes in acidic and alkaline electrolytes: A comparative study on activity and stability. *Catal. Today* **262**, 170–180 (2016).

13.   Cherevko, S. Stability and dissolution of electrocatalysts: Building the bridge between model and "real world" systems. *Curr. Opin. Electrochem.* **8**, 118–125 (2018).

14.   Spöri, C., Kwan, J. T. H., Bonakdarpour, A., Wilkinson, D. P. & Strasser, P. The Stability Challenges of Oxygen Evolving Catalysts: Towards a Common Fundamental Understanding and Mitigation of Catalyst Degradation. *Angew. Chem. Int. Ed.* **56**, 5994–6021 (2017).

15.   Rabe, M. *et al*. Alkaline manganese electrochemistry studied by in situ and operando spectroscopic methods – metal dissolution, oxide formation and oxygen evolution. *Phys Chem Chem Phys* **21**, 10457–10469 (2019).

16.   Roy, C. *et al*. Trends in Activity and Dissolution on RuO_2 under Oxygen Evolution Conditions: Particles versus Well-Defined Extended Surfaces. *ACS Energy Lett.* **3**, 2045–2051 (2018).

17.   Cherevko, S., Geiger, S., Kasian, O., Mingers, A. & Mayrhofer, K. J. J. Oxygen evolution activity and stability of iridium in acidic media. Part 1. – Metallic iridium. *J. Electroanal. Chem.* **773**, 69–78 (2016).

18.   Cherevko, S., Geiger, S., Kasian, O., Mingers, A. & Mayrhofer, K. J. J. Oxygen evolution activity and stability of iridium in acidic media. Part 2. – Electrochemically grown hydrous iridium oxide. *J. Electroanal. Chem.* **774**, 102–110 (2016).

19.   Geiger, S. *et al*. The stability number as a metric for electrocatalyst stability benchmarking. *Nat. Catal.* **1**, 508–515 (2018).

20.   Geiger, S. *et al*. Activity and Stability of Electrochemically and Thermally Treated Iridium for the Oxygen Evolution Reaction. *J. Electrochem. Soc.* **163**, F3132–F3138 (2016).

21.   Grimaud, A. *et al*. Activation of surface oxygen sites on an iridium-based model catalyst for the oxygen evolution reaction. *Nat. Energy* **2**, 16189 (2016).

22.   Kasian, O. *et al*. Degradation of iridium oxides via oxygen evolution from the lattice: correlating atomic scale structure with reaction mechanisms. *Energy Env. Sci* **12**, 3548–3555 (2019).

23.   Zagalskaya, A. & Alexandrov, V. Role of Defects in the Interplay between Adsorbate Evolving and Lattice Oxygen Mechanisms of the Oxygen Evolution Reaction in RuO_2 and IrO_2. *ACS Catal.* **10**, 3650–3657 (2020).

24.   Lee, K., Osada, M., Hwang, H. Y. & Hikita, Y. Oxygen Evolution Reaction Activity in $IrO_x/SrIrO_3$ Catalysts: Correlations between Structural Parameters and the Catalytic Activity. *J. Phys. Chem. Lett.* **10**, 1516–1522 (2019).

25.   Yang, L. *et al*. Efficient oxygen evolution electrocatalysis in acid by a perovskite with face-sharing IrO_6 octahedral dimers. *Nat. Commun.* **9**, 5236 (2018).

26.   Kuo, D.-Y. *et al*. Influence of Strain on the Surface–Oxygen Interaction and the Oxygen Evolution Reaction of $SrIrO_3$. *J. Phys. Chem.* C **122**, 4359–4364 (2018).

27.   Wan, G. *et al*. Amorphization mechanism of $SrIrO_3$ electrocatalyst: How oxygen redox initiates ionic diffusion and structural reorganization. *Sci. Adv.* **7**, eabc7323 (2021).

28.   Chen, Y. *et al*. Exceptionally active iridium evolved from a pseudo-cubic perovskite for oxygen evolution in acid. *Nat. Commun.* **10**, 572 (2019).

29.   Binninger, T. *et al*. Thermodynamic explanation of the universal correlation between oxygen evolution activity and corrosion of oxide catalysts. *Sci. Rep.* **5**, 12167 (2015).

30.   Pourbaix, M. J. N., Van Muylder, J. & De Zoubov, N. Electrochemical properties of the platinum metals. *Platin. Met. Rev.* **3**, 47–53 (1959).

31.   Pearce, P. E. *et al*. Revealing the Reactivity of the Iridium Trioxide Intermediate for the Oxygen Evolution Reaction in Acidic Media. *Chem. Mater.* **31**, 5845–5855 (2019).

32.   Wang, Z., Guo, X., Montoya, J. & Nørskov, J. K. Predicting aqueous stability of solid with computed Pourbaix diagram using SCAN functional. *Npj Comput. Mater.* **6**, 160 (2020).

33.   Kasian, O., Grote, J.-P., Geiger, S., Cherevko, S. & Mayrhofer, K. J. J. The Common Intermediates of Oxygen Evolution and Dissolution Reactions during Water Electrolysis on Iridium. *Angew. Chem. Int. Ed.* **57**, 2488–2491 (2018).

34.   Schalenbach, M. *et al*. The Electrochemical Dissolution of Noble Metals in Alkaline Media. *Electrocatalysis* **9**, 153–161 (2018).

35.   Jovanovič, P. *et al*. Electrochemical Dissolution of Iridium and Iridium Oxide Particles in Acidic Media: Transmission Electron Microscopy, Electrochemical Flow Cell Coupled to Inductively Coupled Plasma Mass Spectrometry, and X-ray Absorption Spectroscopy Study. *J. Am. Chem. Soc.* **139**, 12837–12846 (2017).

36.   Ben-Naim, M. *et al*. Understanding Degradation Mechanisms in $SrIrO_3$ Oxygen Evolution Electrocatalysts: Chemical and Structural Microscopy at the Nanoscale. *Adv. Funct. Mater.* **31**, 2101542 (2021).

37.   Kuwahara, Y. In situ Atomic Force Microscopy study of dissolution of the barite (001) surface in water at 30°C. *Geochim. Cosmochim. Acta* **75**, 41–51 (2011).

38.   Miyata, K. *et al*. Dissolution Processes at Step Edges of Calcite in Water Investigated by High-Speed Frequency Modulation Atomic Force Microscopy and Simulation. *Nano Lett*. **17**, 4083–4089 (2017).

39.   Noiriel, C., Oursin, M., Saldi, G. & Haberthür, D. Direct Determination of Dissolution Rates at Crystal Surfaces Using 3D X-ray Microtomography. *ACS Earth Space Chem*. **3**, 100–108 (2019).

40.   Weber, T. *et al*. Potential-Induced Pitting Corrosion of an $IrO_2(110)$-$RuO_2(110)$/Ru(0001) Model Electrode under Oxygen Evolution Reaction Conditions. *ACS Catal*. **9**, 6530–6539 (2019).

41.   Andersen, C. B. Understanding Carbonate Equilibria by Measuring Alkalinity in Experimental and Natural Systems. *J. Geosci. Educ*. **50**, 389–403 (2002).

42.   Zhao, Y., Vargas-Barbosa, N. M., Hernandez-Pagan, E. A. & Mallouk, T. E. Anodic Deposition of Colloidal Iridium Oxide Thin Films from Hexahydroxyiridate(IV) Solutions. *Small* **7**, 2087–2093 (2011).

43.   Zhao, Y. *et al*. Understanding the Effect of Monomeric Iridium(III/IV) Aquo Complexes on the Photoelectrochemistry of $IrO_x \cdot nH_2O$-Catalyzed Water-Splitting Systems. *J. Am. Chem. Soc*. **137**, 8749–8757 (2015).

44.   Pourbaix, M. *Atlas of Electrochemical Equilibria in Aqueous Solutions*. (National Association of Corrosion Engineers, 1966).

45.   Baeumer, C. *et al*. Tuning electrochemically driven surface transformation in atomically flat $LaNiO_3$ thin films for enhanced water electrolysis. *Nat. Mater*. (2021) doi:10.1038/s41563-020-00877-1.

46.   Powell, C. J. Practical guide for inelastic mean free paths, effective attenuation lengths, mean escape depths, and information depths in x-ray photoelectron spectroscopy. *J. Vac. Sci. Technol. A* **38**, 023209 (2020).

47.   Tanuma, S., Powell, C. J. & Penn, D. R. Calculations of electron inelastic mean free paths. V. Data for 14 organic compounds over the 50–2000 eV range. *Surf. Interface Anal*. **21**, 165–176 (1994).

48.   Jablonski, A. & Powell, C. J. Practical expressions for the mean escape depth, the information depth, and the effective attenuation length in Auger-electron spectroscopy and x-ray photoelectron spectroscopy. *J. Vac. Sci. Technol. A* **27**, 253–261 (2009).

49.   Chambers, S. A. & Du, Y. Experimental determination of electron attenuation lengths in complex materials by means of epitaxial film growth: Advantages and challenges. *J. Vac. Sci. Technol. A* **38**, 043409 (2020).

50.   Högfeldt, E. *Stability Constants of Metal-Ion Complexes: Part A. Inorganic Ligands.* (Pergamon, 1984).

51.   Reardon, E. J. & Armstrong, D. K. Celestite (SrSO$_4$(s)) solubility in water, seawater and NaCl solution. *Geochim. Cosmochim. Acta* **51**, 63–72 (1987).
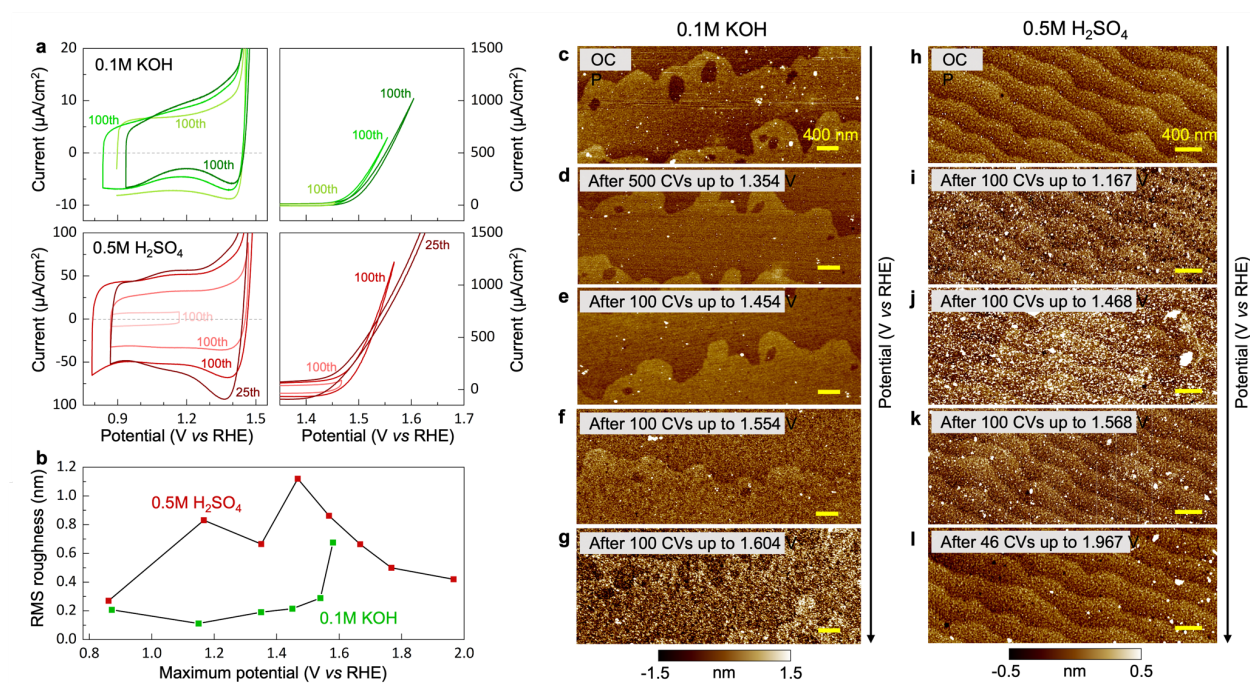
Figure 1. (a) Capacitive (left) and OER (right) regions of the SrIrO$_3$ film after a given number of cycles up to different anodic given potentials measured in the RDE cell. No *iR* correction was made because our samples showed a potential-dependent solid-state junction resistance (see Methods). (b) The root mean square (RMS) roughness after each CV series up to a maximum potential in 0.1M KOH and 0.5M H$_2$SO$_4$. (c-l) Surface roughening during cycling up to increasingly higher potentials in 0.1M KOH and 0.5M H$_2$SO$_4$, corresponding to CV conditions given in (a) and (b) (scale bars are 400 nm). The open-circuit potential, OCP, was near 0.9 V vs. RHE. See Figure S6 and S8 for further data and information.
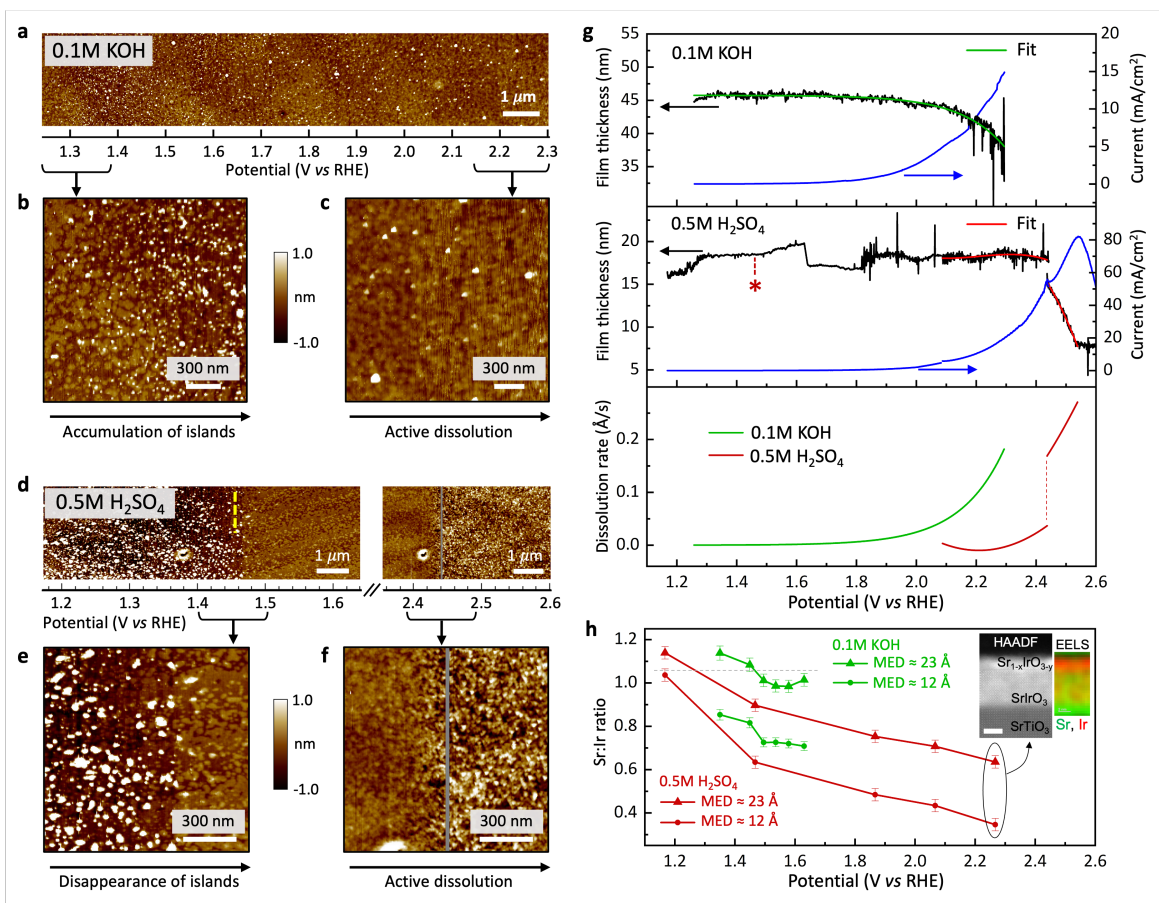
Figure 2. (a) *Operando* EC-AFM measurements of the SrIrO₃ film in 0.1M KOH (see also Figure S9). (b, c) An enlarged region of the AFM image showing (b) the initiation of the potential-dependent surface evolution that generates particulates on the surface without the loss of the step-terraced surface morphology, and (c) the dissolution regime (the image is flattened for clarity). (d) The evolution of the SrIrO₃ film in 0.5M H₂SO₄ (see also Figure S10). (e,f) Disappearance of particulates from the surface and the beginning of active dissolution of Sr₁₋ₓIrO₃. (g) Evolution of the film thickness in 0.1M KOH and 0.5M H₂SO₄ with potential obtained in the *operando* EC-AFM experiment. The dissolution rate is evaluated by fitting the thickness as a function of time (green curve – exponential fit, red curve – 3ʳᵈ degree polynomial fit). The red asterisk marks the potential at which the particulates on the surface in (d) disappear (yellow dashed line). (h) X-ray photoelectron spectroscopy showing Sr depletion at the surface near the OER onset potential for the two electrolytes. MED – mean escape depth. The error bars represent standard deviation in

percentage (derived from the standard deviation of five XPS measurements performed on an as-grown film). The inset shows the HAADF STEM image and EELS map of the film after the *ex-situ* XPS measurements in 0.5M H_2SO_4 revealing a heavily Sr-depleted surface $Sr_{1-x}IrO_{3-y}$ layer. The scale bar is 3nm.
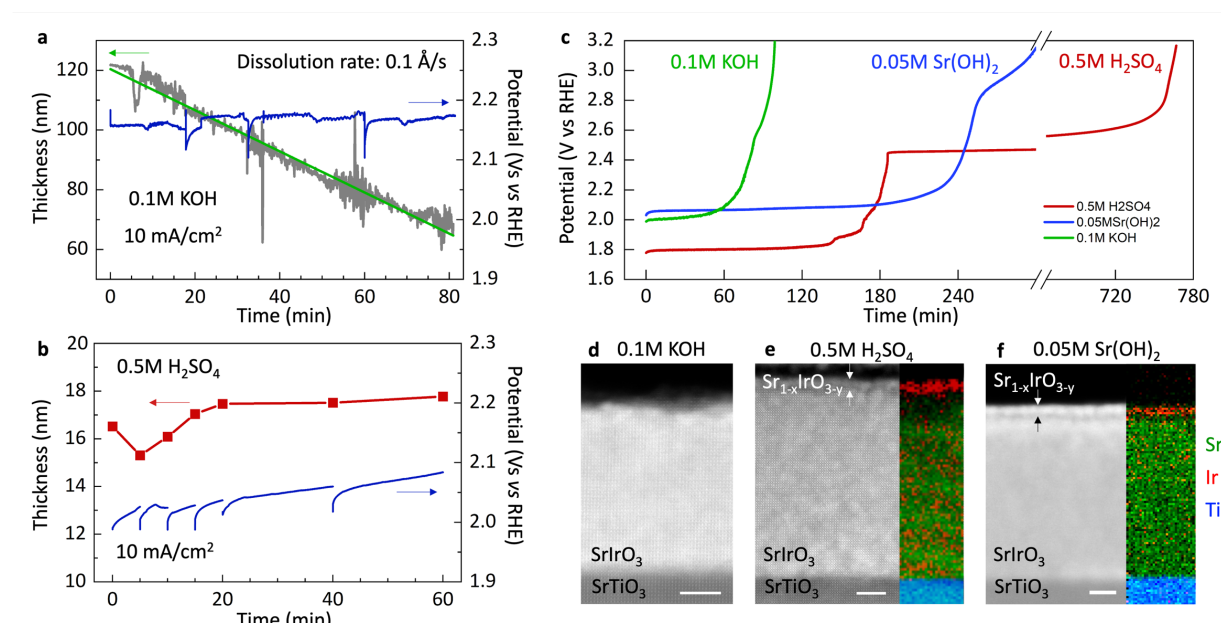

Figure 3. (a-b) Thickness variation of the $SrIrO_3$ film during galvanostatic measurements at 10 mA/cm² in 0.1M KOH and 0.5M H_2SO_4 obtained in *operando* EC-AFM experiments (see more data in Figure S13, S14, S15). **(c)** Evolution of potential in galvanostatic measurements (at 10 mA/cm²) in an RDE cell showing the variation of OER current as electrode films with identical thickness (30 nm) undergo anodic corrosion in different electrolytes. No *iR* correction was made because our samples showed a potential-dependent solid-state junction resistance (see Methods). **(d-f)** HAADF images and EELS maps of the cross sections of the films tested galvanostatically at 10 mA/cm² for 1 h in different electrolytes (scale bar is 5 nm). Colored EELS maps show Sr (green), Ir (red) and Ti (blue) elemental distribution. Because of the difference in dissolution rates in these electrolytes, the starting thickness of the films was not the same.
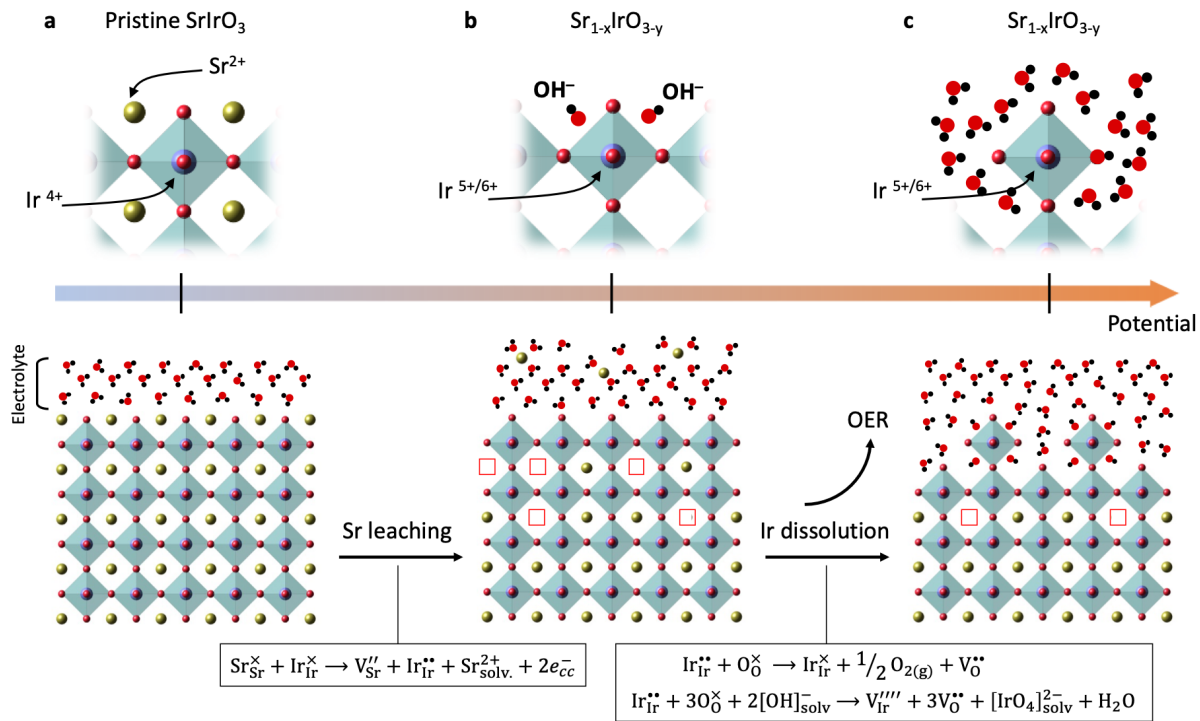
Figure 4. Strontium leaching as a vital reaction step that leads to the perovskite anodic degradation in an alkaline medium: (a) Pristine SrIrO₃ surface in contact with electrolyte; (b) Sr leaching leads to the formation of Sr₁₋ₓIrO₃ with a higher oxidation state of Ir within the near-surface layer; (c) Ir⁵⁺/⁶⁺ either reduces chemically to Ir⁴⁺ while evolving O₂ or dissolves via hydroxylation and formation of [IrO₄]²⁻ species.

Methods

Thin film preparation and characterization. Thin films of $SrIrO_3$ were grown by pulsed laser deposition (PLD/MBE 2300, PVD Products) on 10x10 mm^2 (001) Nb-doped $SrTiO_3$ (0.5 wt% doping) (Shinkosha Co., Japan) using $SrIrO_3$ target (Toshima Manufacturing, Japan). All substrates were first etched with buffered HF solution (pH = 4.5) and annealed at 950 °C under Argon flow for 2 hours to restore high-quality step terraces. The growth temperature was 700 °C under oxygen pressure of 30 mTorr (some samples were grown under 15 mTorr). The target to substrate distance was 84 mm, the laser fluence was 2 J/cm^2. The growth was monitored *in situ* using a RHEED system (TorrRHEED, Staib Instruments) operated at 35 kV (1.5 mA). The samples with the $SrIrO_3$-$SrTiO_3$ step were prepared through the following steps: (i) a small area on the substrate was covered with acetone-soluble photoresist (Megaposit SPR3612); (ii) an amorphous layer (20-30nm) of water-soluble $Sr_3Al_2O_6$ was grown at room temperature in the PLD from the $Sr_3Al_2O_6$ in-house prepared target; (iii) the photoresist was then removed using acetone, leaving a clean area on the substrate; (iv) $SrIrO_3$ layer was grown on top of the entire sample under conditions mentioned above; (v) finally, the sample was immersed in water for several hours and lightly sonicated to dissolve $Sr_3Al_2O_6$ and remove the $SrIrO_3$ layer grown above it but leaving the $SrIrO_3$ layer in the area previously protected by the photoresist. Such samples had a small area (0.1-0.3 mm^2) of the $SrIrO_3$ film on a large-area substrate and were used in the majority of electrochemical AFM experiments. Although we did not notice any thickness dependence of degradation, thicker films were used in EC-AFM experiments conducted in KOH because of higher dissolution rates of $SrIrO_3$ in this electrolyte. X-ray diffraction and X-ray reflectivity of thicker films were collected using PANalytical X'Pert PRO diffractometer equipped with a double monochromator and operating in the parallel-beam geometry.

Transmission electron microscope specimens were prepared by focused ion beam lift-out technique using a Thermofisher Scientific Helios UC instrument operated at 30 kV at the beginning of preparation, followed by 5 and 2 kV for the final cleaning. The HAADF and EELS images were collected with a Thermofisher Scientific (formerly FEI) image-corrected Titan 80-300 environmental TEM operated at 300 kV, equipped with a Gatan Imaging Filter Quantum 965 ER. Another set of specimens were analyzed with a Thermofisher Scientific probe-corrected Themis Z microscope operated at 80 kV and equipped with a Gatan Imaging Filter Continuum 1065 ER.

The air-free XPS characterization was performed with a PHI Versa Probe (Physical Electronics Inc.) with Al Kα X-ray illumination, a pass energy of 23.5 eV and at various photoemission angles without neutralization. The samples were first tested electrochemically in the RDE cell inside a nitrogen-filled glovebox and transferred to XPS in a transfer vessel without air exposure. The Sr:Ir stoichiometry was calculated using integrated intensity of the respective peaks after subtraction of the Shirley background in CasaXPS and using the sensitivity factors of 5.7772 (Sr) and 16.1333 (Ir). The mean escape depth was defined through the inelastic mean free path (IMFP) of the photoelectrons λ and the photoemission angle θ through $d = \lambda \times \cos \theta$.[46] IMFP was calculated to be 23.8 Å for Sr and 24.7 Å for Ir using QUASES-IMFP-TPP2M.[47] This isotropic approach uses the straight-line approximation[48], as is suitable in the absence of well-characterized, material-specific angle-dependent effective attenuation lengths. For a full description of the information depth in photoemission, the readers are referred to the literature[46,48,49].

Electrochemical measurements. Electrochemical measurements of the thin films were performed using a rotating disk electrode (RDE, Pine Research) setup at rotation rates of 1000-1500 r.p.m. A PTFE cell was used and the electrolyte was never exposed to glass. Only the front side of the film was exposed to the electrolyte (film area is 10x10mm^2, while the electrolyte-contacted area is circular with a diameter of 7.5 mm), and the potential was controlled using a BioLogic SP-300 potentiostat. On the electrolyte side, a film area of 0.75 mm diameter was exposed to the electrolyte and sealed using an O-ring (FFKM, Marco Rubber). Electrical contact was made from the back of the substrate, where the Ti(5 nm) and Pt(50-100 nm) layers were deposited beforehand. The O_2-saturated electrolyte solutions used in the experiments were prepared using the following chemicals: KOH pellets (Sigma-Aldrich, Semiconductor grade, 99.99%), concentrated H_2SO_4 (Honeywell, TraceSELECT™ Ultra), $Sr(OH)_2 \cdot 8H_2O$ (Alfa Aesar, 99%). A set of carefully maintained Hg/HgO reference electrodes (CHI152, CH Instruments) filled with 1M KOH were used in the experiments involving alkaline and neutral electrolytes, with a separate "master" electrode that was used for calibration purposes (typical deviations were within 1-3 mV). The 1M KOH electrolyte inside the Hg/HgO electrode was replaced after each measurement in the chemically non-native $Sr(OH)_2$ electrolyte. Similarly, Hg/Hg_2SO_4 reference electrodes (RREF0025, Pine Research) were used in the 0.5M H_2SO_4. We found that our heterostructures exhibit a solid-state film-substrate junction resistance that is potential-dependent.

This makes an accurate correction for resistance difficult As a result, no correction for the resistance-induced potential drop was done for all samples (the data are as measured). Unless stated otherwise, the solution resistances were (1) in the RDE cell: 54 Ohm in 0.1M KOH and 8 Ohm in 0.5M H_2SO_4, and (2) in the AFM cell: ~16-20 Ohm in 0.1M KOH and ~4 Ohm in 0.5M H_2SO_4. The concentration of Sr^{2+} in equilibrium with $SrCO_3$ was calculated using the solubility constant K_{sp} ($SrCO_3$) = 5.6×10^{-10} (ref [50]) and with $SrSO_4$ using the solubility constant K_{sp}($SrSO_4$) = 2.33×10^{-7} (ref [51]).

Electrochemical Atomic Force Microscopy. Atomic Force Microscopy was performed using Oxford Instruments Asylum Cypher ES scanning probe microscope and a modified liquid cell. The scans were recorded in a tapping mode using Olympus AC55TS tips (radius ~7 nm) that were excited photothermally (blueDriveTM) on the gold-coated reflex side. These tips can operate in liquid at high resonance frequency (~ 1 MHz), have a stable resonance and therefore are ideal for high-resolution imaging. In the scanning process, the phase was kept close to 70-80% to make sure the tip operated in a repulsive regime without a significant mechanical force. The Asylum software package implemented into Igor Pro was used for flattening and correcting the AFM images. When particulates appeared on the surface, depending on the tip-sample interaction, the tip could go afloat. When such lines were occasional, they were removed from the scan using the "Erase line" function under "Modify Panel" in the Asylum software. When the lines were not occasional, they were left as is.

Electrochemical AFM experiments were done in the original liquid cell from Asylum Research but modified to incorporate all three electrodes, one of which was a real reference electrode (Hg/HgO for 0.1M KOH and Hg/Hg_2SO_4 for 0.5M H_2SO_4). During the OER reaction inside the AFM cell, a continuous electrolyte flow was maintained using a "push-pull" combination of two syringe pumps (PHD ULTRA, Harvard Apparatus) at a rate of 50-500 μL min^{-1} depending on the current.

Associated Content

Supporting Information contains additional figures and equation sets, including EC-AFM results, XPS, and X-ray diffractograms.

Abbreviations

EC-AFM – electrochemical atomic force microscopy

OER – oxygen evolution reaction

RHE – reversible hydrogen electrode

LSV – linear sweep voltammetry

XPS – X-ray photoelectron spectroscopy

MED – mean escape depth

HAADF STEM – high-angle annular dark-field scanning transmission electron microscopy

EELS – electron energy loss spectroscopy

Author Information Notes

[5]Present address: Division for Research with Neutrons and Muons, Paul Scherrer Institute, 5232 Villigen, Switzerland

* Corresponding authors: andrei.akbasheu@psi.ch